

Horizontally viscous effects in a tidal basin: extending Taylor's problem

P. C. ROOS¹† AND H. M. SCHUTTELAARS²

¹Water Engineering and Management, Faculty of Engineering Technology, University of Twente,
PO Box 217, 7500 AE Enschede, The Netherlands

²Department of Applied Mathematical Analysis, Delft University of Technology, PO Box 5031,
2600 GA Delft, The Netherlands

(Received 28 November 2008; revised 20 July 2009; accepted 22 July 2009; first published online
27 October 2009)

The classical problem of Taylor (*Proc. Lond. Math. Soc.*, vol. 20, 1921, pp. 148–181) of Kelvin wave reflection in a semi-enclosed rectangular basin of uniform depth is extended to account for horizontally viscous effects. To this end, we add horizontally viscous terms to the hydrodynamic model (linearized depth-averaged shallow-water equations on a rotating plane, including bottom friction) and introduce a no-slip condition at the closed boundaries.

In a straight channel of infinite length, we obtain three types of wave solutions (normal modes). The first two wave types are viscous Kelvin and Poincaré modes. Compared to their inviscid counterparts, they display longitudinal boundary layers and a slight decrease in the characteristic length scales (wavelength or along-channel decay distance). For each viscous Poincaré mode, we additionally find a new mode with a nearly similar lateral structure. This third type, entirely due to viscous effects, represents evanescent waves with an along-channel decay distance bounded by the boundary-layer thickness.

The solution to the viscous Taylor problem is then written as a superposition of these normal modes: an incoming Kelvin wave and a truncated sum of reflected modes. To satisfy no slip at the lateral boundary, we apply a Galerkin method. The solution displays boundary layers, the lateral one at the basin's closed end being created by the (new) modes of the third type. Amphidromic points, in the inviscid and frictionless case located on the centreline of the basin, are now found on a line making a small angle to the longitudinal direction. Using parameter values representative for the Southern Bight of the North Sea, we finally compare the modelled and observed tide propagation in this basin.

1. Introduction

Tidal dynamics plays an important role in large-scale semi-enclosed basins like the North Sea. Coastal safety, navigation and ecology are all affected by the tide, directly through fluctuating water levels and oscillatory currents, as well as indirectly through the presence and dynamics of tide-induced bedforms like sandbanks and sandwaves (Dyer & Huntley 1999). To study the propagation of a tidal wave from a process-based modelling perspective, two approaches exist: (i) numerical models

† Email address for correspondence: p.c.roos@utwente.nl

with realistic geometries to reproduce and predict tidal observations and (ii) idealized models to obtain insight into physical mechanisms.

In the literature, many models of the first type can be found (Sinha & Pingree 1997; Fang *et al.* 1999; Cai *et al.* 2006). Usually these models contain a horizontal eddy viscosity, which represents lateral friction. Since this parameter is difficult to quantify, it is often treated as an overall tuning parameter to improve model performance. The horizontal viscosity affects the energy transfer among tide constituents (in a nonlinear model) as well as the numerical stability. In addition, the numerical schemes usually introduce numerical/artificial diffusion, which obscures the role of the physical viscosity in the model results.

To understand the effects of a horizontal viscosity on various aspects of tide dynamics, we adopt a model of the second type, with a strongly simplified geometry: a semi-enclosed rectangular basin of uniform depth and width. The problem of (coastally trapped) Kelvin wave reflection in such a basin geometry was first studied by Taylor (1921), using an inviscid hydrodynamic model, i.e. depth-averaged linearized shallow-water equations on a rotating plane. The solution is a superposition of an incoming Kelvin wave, a reflected Kelvin wave and an infinite series of Poincaré modes, generated at the closed end to satisfy the no-normal flow condition. The resulting amphidromic system displays elevation and current amphidromic points alternatingly on the centreline of the basin, provided the channel is sufficiently narrow for all Poincaré modes to be evanescent (LeBlond & Mysak 1978). Taylor's strongly idealized model qualitatively reproduces the main features of tides in large-scale basins like the North Sea (Brown 1987).

Several extensions of Taylor's model can be found in the literature. Following Proudman (1941), Hendershott & Speranza (1971) replaced the no-normal flow condition at the closed end with a partially absorbing one, which reduces the amplitude of the reflected Kelvin wave and shifts the amphidromes away from the centreline. To estimate the absorption coefficients for the Adriatic Sea and the Gulf of California, two Kelvin waves were fit to tide observations in the central parts of these basins. Alternatively, Rienecker & Teubner (1980) incorporated a linear bottom friction formulation (vertical friction), which causes damping of the (Kelvin) waves as they propagate, shifting the amphidromes on to a straight line making a small angle with the boundaries. The positions of current and elevation amphidromic points have been investigated in detail by Xia, Carbajal & Südermann (1995), Carbajal (1997) and Rizal (2002). To mimic the effects of the Dover strait on the North Sea, Brown (1987, 1989) added an oscillatory along-channel flow at the closed end. The three-dimensional flow structure has been investigated numerically by Davies & Jones (1995, 1996) and (semi-)analytically by Winant (2007), who developed a three-dimensional model of tidal flow in narrow estuaries with a parabolic lateral bottom profile.

In this study, we will extend the Taylor problem to account for horizontally viscous effects (lateral friction), which has not been addressed so far. How do they affect the properties of a Kelvin wave and the way in which it is reflected at the basin's closed end, as well as the resulting amphidromic system? And how do horizontally viscous effects compare to those of another dissipation mechanism, namely bottom friction? Analogous to Taylor's approach outlined above, our model allows for a (semi-) analytical solution, written as a superposition of wave solutions in an infinitely long channel. Our analysis therefore also describes the effects of viscosity on the existence and properties of these individual modes, such as the Kelvin mode. The method

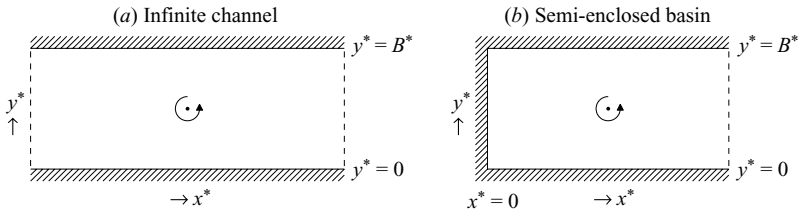


FIGURE 1. Definition sketch of the geometry: (a) infinite channel with longitudinal boundaries at $y^* = 0, B^*$; (b) semi-enclosed basin with an additional lateral boundary at $x^* = 0$.

excludes numerical diffusion, while resolving all relevant length scales associated with boundary layers and the interior of the domain. Unlike the three-dimensional model of Winant (2007), our depth-averaged approach is not restricted to narrow basins.

This paper is organized as follows. First, §2 contains the model formulation, including horizontally viscous terms, a linear bottom-friction formulation and no-slip boundary conditions. Next, in §3 we derive the normal modes, i.e. wave solutions proportional to $\exp(i[\sigma^* t^* - k^* x^*])$. In our forced time-periodic problem, we emphasize that the angular frequency σ^* is fixed and real, whereas the wavenumber k^* is complex (Ripa & Zavala-Garay 1999). This contrasts e.g. with the study of Davey, Hsieh & Wajsbowicz (1983) of viscous Kelvin waves in which k^* is real and σ^* complex, which is suitable for initial value problems. Our analysis identifies viscous Kelvin and viscous Poincaré modes, as well as a new type of mode. (In our study, the terms viscous/inviscid are used to denote the presence/absence of horizontally viscous effects, and frictional/frictionless refers to the presence/absence of bottom friction.) The properties of these modes are analysed in §4, adopting parameter values that are typical for the Southern Bight of the North Sea. In §5 a superposition of normal modes is considered to solve the viscous Taylor problem, using a Galerkin technique. We then compare our idealized model results with tide observations from the North Sea. Finally, the conclusions are given in §6.

2. Model

Consider a tidal wave of angular frequency σ^* (dimensional quantities are denoted with an asterisk) and typical elevation amplitude Z^* (several metres) in a rectangular section of a rotating channel of uniform depth H^* (tens of metres) and width B^* (tens to hundreds of kilometres). We define a three-dimensional coordinate system with horizontal components x^* and y^* and a vertical coordinate z^* pointing upward from mean sea level. We now consider two geometries, as depicted in figure 1. The first is an open channel of infinite length with longitudinal channel boundaries at $y^* = 0$ and $y^* = B^*$ (figure 1a). The second is the actual geometry of Taylor's problem: a semi-enclosed basin with similar longitudinal boundaries and in addition a closed lateral boundary at $x^* = 0$ (figure 1b). The free-surface displacement is denoted by $z^* = \zeta^*$, and we introduce depth-averaged flow velocity components u^* and v^* in the x^* - and y^* -direction, respectively.

Conservation of momentum and mass is then expressed by the nonlinear depth-averaged shallow-water equations, according to

$$\frac{\partial u^*}{\partial t^*} + u^* \frac{\partial u^*}{\partial x^*} + v^* \frac{\partial u^*}{\partial y^*} - f^* v^* + \frac{r^* u^*}{H^* + \zeta^*} = -g^* \frac{\partial \zeta^*}{\partial x^*} + v^* \left[\frac{\partial^2 u^*}{\partial x^{*2}} + \frac{\partial^2 u^*}{\partial y^{*2}} \right], \quad (2.1)$$

$$\frac{\partial v^*}{\partial t^*} + u^* \frac{\partial v^*}{\partial x^*} + v^* \frac{\partial v^*}{\partial y^*} + f^* u^* + \frac{r^* v^*}{H^* + \zeta^*} = -g^* \frac{\partial \zeta^*}{\partial y^*} + v^* \left[\frac{\partial^2 v^*}{\partial x^{*2}} + \frac{\partial^2 v^*}{\partial y^{*2}} \right], \quad (2.2)$$

$$\frac{\partial \zeta^*}{\partial t^*} + \frac{\partial [(H^* + \zeta^*)u^*]}{\partial x^*} + \frac{\partial [(H^* + \zeta^*)v^*]}{\partial y^*} = 0. \quad (2.3)$$

Here, t^* is time, g^* the gravitational acceleration, $f^* = 2\Omega^* \sin \vartheta$ a Coriolis parameter (with latitude ϑ and $\Omega^* = 7.292 \times 10^{-5} \text{ rad s}^{-1}$ the angular frequency of the Earth's rotation), r^* a linear bottom-friction coefficient and ν^* the horizontal eddy viscosity. Typical parameter values will be detailed in §4.1.

We impose a no-slip condition at the closed boundaries,

$$u^* = v^* = 0, \quad (2.4)$$

to be satisfied at $y^* = 0, B^*$ for all x^* (for the channel geometry in figure 1a) or at $y^* = 0, B^*$ for $x^* \geq 0$ and at $x^* = 0$ for $0 \leq y^* \leq B^*$ (for the semi-enclosed basin geometry in figure 1b). The inviscid case ($\nu^* = 0$) admits only a no-normal flow condition. The Taylor problem is forced by a Kelvin wave, coming in from $+\infty$. The existence and properties of such a viscous Kelvin wave are investigated in §3.

Now let us introduce non-dimensional quantities

$$\zeta = \frac{\zeta^*}{Z^*}, \quad (u, v) = \frac{(u^*, v^*)}{U^*}, \quad (x, y) = K^*(x^*, y^*), \quad t = \sigma^* t^*, \quad (2.5)$$

with typical velocity scale $U^* = Z^* \sqrt{g^*/H^*}$ and reference wavenumber $K^* = \sigma^*/\sqrt{g^*H^*}$, both associated with a classical Kelvin wave, inviscid and without bottom friction. At lowest order in the gravitational Froude number, i.e. at $O(Fr^0)$, with

$$Fr = \frac{U^*}{\sqrt{g^*H^*}} \quad \left(= \frac{Z^*}{H^*} \right), \quad (2.6)$$

we obtain the following set of linear model equations:

$$\frac{\partial u}{\partial t} - f v + r u = -\frac{\partial \zeta}{\partial x} + \nu \left[\frac{\partial^2 u}{\partial x^2} + \frac{\partial^2 u}{\partial y^2} \right], \quad (2.7)$$

$$\frac{\partial v}{\partial t} + f u + r v = -\frac{\partial \zeta}{\partial y} + \nu \left[\frac{\partial^2 v}{\partial x^2} + \frac{\partial^2 v}{\partial y^2} \right], \quad (2.8)$$

$$\frac{\partial \zeta}{\partial t} + \frac{\partial u}{\partial x} + \frac{\partial v}{\partial y} = 0. \quad (2.9)$$

Here we have introduced a dimensionless Coriolis parameter $f = f^*/\sigma^*$ (equal to the inverted Rossby number), a dimensionless friction coefficient $r = r^*/(H^*\sigma^*)$ and a dimensionless viscosity $\nu = \sigma^*\nu^*/(g^*H^*)$. The no-slip condition (2.4) reads $u = v = 0$, to be satisfied at the closed boundaries $y = 0, B$ where $B = K^*B^*$ denotes the dimensionless channel/basin width (and, for the basin geometry, also at $x = 0$).

The system of linear equations (2.7)–(2.9) can be rewritten into so-called polarization equations, expressing the individual velocity components in terms of the free-surface

elevation ζ only (see e.g. Pedlosky 1982, §3.6, for the inviscid and frictionless case). The viscous polarization equations are given by

$$(\mathcal{L}^2 + f^2)u = -\left(\mathcal{L}\left[\frac{\partial\zeta}{\partial x}\right] + f\frac{\partial\zeta}{\partial y}\right), \quad (\mathcal{L}^2 + f^2)v = -\left(\mathcal{L}\left[\frac{\partial\zeta}{\partial y}\right] - f\frac{\partial\zeta}{\partial x}\right). \quad (2.10)$$

Here, we have defined the differential operator $\mathcal{L} = \partial/\partial t + r - \nu\nabla^2$, with Laplace operator $\nabla^2 = \partial^2/\partial x^2 + \partial^2/\partial y^2$. Next, substitution of these results into the continuity equation (2.9) provides a single fourth-order partial differential equation for ζ , referred to as the viscous Klein–Gordon equation:

$$(\mathcal{L}^2 + f^2)\frac{\partial\zeta}{\partial t} - \mathcal{L}\nabla^2\zeta = 0. \quad (2.11)$$

3. Wave solutions in an infinite channel

Let us represent the solution as $\phi = (\zeta, u, v)$. For the infinite channel geometry of figure 1(a), we now proceed by seeking solutions of the form

$$\phi(x, y, t) = \hat{\phi}(y) \exp(i[t - kx]) + \text{c.c.}, \quad \hat{\phi}(y) = (\hat{\zeta}(y), \hat{u}(y), \hat{v}(y)), \quad (3.1)$$

with lateral structures $\hat{\zeta}(y)$, $\hat{u}(y)$ and $\hat{v}(y)$, respectively. The wavenumber $k = k_{re} + ik_{im}$ is to be obtained from the subsequent analysis. Without loss of generality, we restrict our attention to wavenumbers with $k_{im} \leq 0$, i.e. to wave solutions that remain bounded in the positive x -direction. By symmetry, wave solutions that remain bounded in the negative x -direction can then be found from applying the transformations $k \mapsto -k$, $y \mapsto B - y$ and $(u, v) \mapsto (-u, -v)$.

Let us proceed analogously to the analysis of Pedlosky (1982, §3.9) but include both bottom friction and viscous effects. It follows from (3.1) that the time derivative and the space derivative in the longitudinal direction now become algebraic: $\partial/\partial t = i$ and $\partial/\partial x = -ik$. In particular, we may write $\mathcal{L} = i\gamma^2 + \nu(k^2 - \partial^2/\partial y^2)$ with $\gamma^2 = 1 - ir$. The viscous Klein–Gordon equation (2.11) reduces to the following fourth-order ordinary differential equation for $\hat{\zeta}(y)$:

$$a\frac{\partial^4\hat{\zeta}}{\partial y^4} + b\frac{\partial^2\hat{\zeta}}{\partial y^2} + c\hat{\zeta} = 0, \quad (3.2)$$

with complex coefficients

$$\left. \begin{aligned} a &= \nu(1 + i\nu), \\ b &= -i\gamma^2(1 + 2i\nu) - 2\nu(1 + i\nu)k^2, \\ c &= i(f^2 - \gamma^4) + i\gamma^2(1 + 2i\nu)k^2 + \nu(1 + i\nu)k^4. \end{aligned} \right\} \quad (3.3)$$

Equation (3.2) leads to exponential solutions of the general form

$$\hat{\zeta}(y) = Z_1 \exp(-\alpha y) + Z_2 \exp(-\beta y) + Z_3 \exp(\alpha[y - B]) + Z_4 \exp(\beta[y - B]), \quad (3.4)$$

with $\alpha = \alpha_{re} + i\alpha_{im}$ and $\beta = \beta_{re} + i\beta_{im}$ the roots of the characteristic polynomial $a\lambda^4 + b\lambda^2 + c = 0$, where we have taken without loss of generality the roots with a positive real part, i.e. $\alpha_{re} \geq 0$ and $\beta_{re} \geq 0$. By adopting (3.4), we implicitly assume that the roots α and β are distinct and non-zero.

The polarization equations (2.10) show that the lateral structures $\hat{u}(y)$ and $\hat{v}(y)$ of the flow field must have a form similar to (3.4) but involving different coefficients U_j and V_j ($j = 1, 2, 3, 4$). The boundary conditions, requiring $u = v = 0$ at $y = 0$ and

$y = B$, now lead to a linear system $\mathbf{A}\mathbf{z} = 0$, with

$$\mathbf{A} = \begin{bmatrix} P_{\alpha-} & P_{\beta-} & P_{\alpha+}e^{-\alpha B} & P_{\beta+}e^{-\beta B} \\ Q_{\alpha-} & Q_{\beta-} & Q_{\alpha+}e^{-\alpha B} & Q_{\beta+}e^{-\beta B} \\ P_{\alpha-}e^{-\alpha B} & P_{\beta-}e^{-\beta B} & P_{\alpha+} & P_{\beta+} \\ Q_{\alpha-}e^{-\alpha B} & Q_{\beta-}e^{-\beta B} & Q_{\alpha+} & Q_{\beta+} \end{bmatrix}, \quad \mathbf{z} = \begin{bmatrix} Z_1 \\ Z_2 \\ Z_3 \\ Z_4 \end{bmatrix}. \quad (3.5)$$

In (3.5), we have defined the following scalar quantities:

$$P_{\alpha\pm} = \frac{-(-\mathcal{L}_\alpha ik \pm f\alpha)}{\mathcal{L}_\alpha^2 + f^2}, \quad Q_{\alpha\pm} = \frac{-(\pm\mathcal{L}_\alpha\alpha + fik)}{\mathcal{L}_\alpha^2 + f^2}, \quad (3.6)$$

in which $\mathcal{L}_\alpha = i\gamma^2 + \nu(k^2 - \alpha^2)$. By replacing α with β in the above, we analogously define $P_{\beta\pm}$, $Q_{\beta\pm}$ and \mathcal{L}_β .

Non-trivial wave solutions only exist when the solvability condition

$$\det \mathbf{A}(k, \alpha(k), \beta(k)) = 0 \quad (3.7)$$

is satisfied. In (3.7), we have emphasized the direct and indirect dependencies on the wavenumber k . As it turns out, the solvability condition (3.7) introduces three types of wave solutions: (i) the viscous Kelvin mode (denoted with the subscript 0), (ii) the viscous Poincaré modes (denoted with the subscripts $m = 1, 2, \dots$) and (iii) a new type of mode ($m = -1, -2, \dots$). An analytical way of investigating these modes involves an expansion of the three quantities (k_m, α_m, β_m) as a power series in $\nu^{1/2}$, possibly including a negative power:

$$k_m = [k_{m,-1}\nu^{-1/2}] + k_{m,0} + \nu^{1/2}k_{m,1} + \nu k_{m,2} + O(\nu^{3/2}), \quad (3.8)$$

$$\alpha_m = \alpha_{m,0} + \nu^{1/2}\alpha_{m,1} + \nu\alpha_{m,2} + O(\nu^{3/2}), \quad (3.9)$$

$$\beta_m = \beta_{m,-1}\nu^{-1/2} + \beta_{m,0} + \nu^{1/2}\beta_{m,1} + \nu\beta_{m,2} + O(\nu^{3/2}). \quad (3.10)$$

Subsequently considering the equations for α_m and β_m and the solvability condition at increasing powers of $\nu^{1/2}$, the coefficients $k_{m,j}$, $\alpha_{m,j}$ and $\beta_{m,j}$ are determined in a systematic way (Appendix A). It is not guaranteed that the expansion converges. Furthermore, the error induced by truncation is unknown. The first term in (3.8) has been put between brackets because the leading term for the wavenumber is only for the new type of mode ($m < 0$) proportional to $\nu^{-1/2}$. For the viscous Kelvin and Poincaré modes ($m \geq 0$), we find $k_{m,-1} = 0$ and $k_{m,0} \neq 0$, making the leading term in (3.8) proportional to ν^0 . Note that inviscid Kelvin and Poincaré modes can then be recovered by setting $\nu = 0$, reducing (3.8) and (3.9) to $k = k_{m,0}$ and $\alpha = \alpha_{m,0}$. (The expressions for $k_{m,0}$ and $\alpha_{m,0}$ are given in Appendix A.)

In the next sections, the analytically obtained k -values are used as the starting point for a numerical search routine in which the absolute value of the determinant $|\det \mathbf{A}(k, \alpha(k), \beta(k))|$ is minimized while varying the wavenumber k . This leads to accurate values of k and the other coefficients involved.

4. Results: properties of wave solutions

4.1. Parameter settings

Now we will investigate the properties of the wave solutions derived in the previous section. As a reference case, we use parameter values typical for the semi-diurnal lunar tide ('M2') in the Southern Bight of the North Sea (table 1). Hence, a 150 km wide basin is considered, with a 25 m depth at a latitude of 52° north. The value of the tidal elevation amplitude Z^* in table 1 is based on the study of the North Sea by

Parameter	Symbol	Value
Basin width	B^*	150 km
Basin depth	H^*	25 m
Maximum elevation amplitude (at the coast)	Z^*	1.5 m
Latitude	ϑ	52° north
Angular frequency of the M2 tide	σ^*	1.41×10^{-4} rad s $^{-1}$
Bottom-friction coefficient	r^*	1.2×10^{-3} m s $^{-1}$
Horizontal eddy viscosity	ν^*	2.0×10^3 m 2 s $^{-1}$
Typical velocity scale (maximum at the coast)	U^*	0.94 m s $^{-1}$
Basin width (dimensionless)	B	1.35 –
Coriolis parameter (dimensionless)	f	0.82 –
Bottom-friction coefficient (dimensionless)	r	0.34 –
Horizontal eddy viscosity (dimensionless)	ν	1.14×10^{-3} –
Gravitational Froude number	Fr	0.06 –

TABLE 1. Overview of parameter values, typical for the Southern Bight of the North Sea.

Sinha & Pingree (1997), from which we also take the value of the horizontal eddy viscosity ν^* . Furthermore, the value of the friction parameter r^* is based on Lorentz' linearization of a quadratic friction law (Zimmerman 1982):

$$r^* = \frac{8}{3\pi} C_D U_{avg}^*, \quad U_{avg}^* = \frac{1}{B^*} \int_0^{B^*} U^* \exp\left(\frac{-y^*}{R^*}\right) dy^*, \quad (4.1)$$

with drag coefficient $C_D = 2.5 \cdot 10^{-3}$ and typical velocity amplitude $U_{avg}^* = 0.57$ m s $^{-1}$, here obtained as the lateral average of the along-channel flow amplitude of a classical Kelvin wave (Pedlosky 1982, §3.9). For our channel geometry, such an inviscid and frictionless wave is characterized by a typical velocity scale $U^* = Z^* \sqrt{g^*/H^*} = 0.94$ m s $^{-1}$ already introduced in §2 and by a Rossby deformation radius $R^* = (g^* H^*)^{1/2} / f^* = 136$ km.

Figure 2 shows the wavenumbers k_m of the modes in the complex plane, i.e. the solutions to the solvability condition (3.7). We particularly see what happens when, starting from the inviscid and frictionless case, dissipation is added to the system. For $r^* = 0$ and $\nu^* = 0$, the wavenumbers of the Kelvin mode (k_0) and the Poincaré modes (k_m with $m > 0$) are denoted by small squares in figure 2. Adding bottom friction ($r^* = r_{ref}^*$ while $\nu^* = 0$) causes these wavenumbers to shift slightly in the complex plane, as denoted by the crosses. For the Kelvin mode and the first Poincaré mode, this shift can best be seen from the zoomed image in figure 2(b). When we also add horizontally viscous effects ($r^* = r_{ref}^*$ and $\nu^* = \nu_{ref}^*$), two changes occur (circles). First, the wavenumbers of the Kelvin and Poincaré modes experience a further shift in the complex plane, which will be investigated in §§4.2 and 4.3. Second, the new type of mode emerges (k_m with $m < 0$; also see figure 2c), which will be investigated in §4.4.

4.2. Viscous Kelvin mode

Figure 3 shows snapshots of the elevation and flow field of the Kelvin mode, for different parameter settings. The quantitative properties of the Kelvin mode are summarized in table 2, showing the reference case (top row) and the case without dissipation (second row) and separately considering the effects of variations in bottom friction and horizontal viscosity. Apart from the dimensionless characteristics derived in §3 (wavenumber k_0 , coefficients α_0 and β_0), the following dimensional and dimensionless quantities are tabulated.

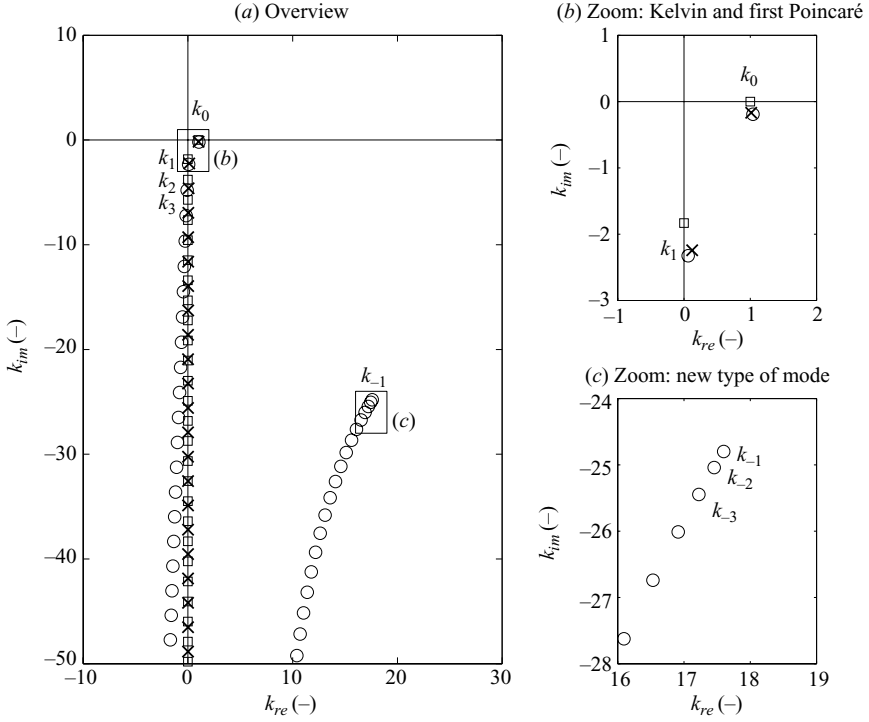


FIGURE 2. Wavenumbers k_m , plotted in the complex wavenumber plane: (a) overview, (b) zoom of the Kelvin and first Poincaré modes, (c) zoom of the new type of mode. Three scenarios are plotted, based on the parameter values in table 1: no dissipation (squares), bottom friction only (crosses) and both bottom friction and horizontally viscous effects (circles).

r^*/r_{ref}^* (-)	ν^*/ν_{ref}^* (-)	k_0 (-)	α_0 (-)	β_0 (-)	L^* (km)	R^* (km)	D (-)	δ_{lat}^* (km)	Δy_{amph}^* (km)
1	1	1.040 - 0.193i	0.809 + 0.093i	24.7 + 17.6i	671	137	0.31	4.5	-80
0	0	1	0.82	-	698	136	1	-	0
0	1	1.024 - 0.026i	0.850 - 0.031i	20.9 + 20.9i	681	131	0.85	5.3	-10
0.01	1	1.024 - 0.027i	0.850 - 0.029i	20.9 + 20.8i	681	131	0.85	5.3	-11
0.1	1	1.025 - 0.043i	0.850 - 0.017i	21.3 + 20.5i	681	131	0.77	5.2	-17
0.5	1	1.029 - 0.110i	0.837 + 0.035i	22.8 + 19.2i	678	133	0.51	4.9	-45
1	1	1.040 - 0.193i	0.809 + 0.093i	24.7 + 17.6i	671	137	0.31	4.5	-80
2	1	1.077 - 0.348i	0.726 + 0.175i	28.8 + 15.1i	648	153	0.13	3.9	-155
10	1	1.533 - 1.154i	0.304 + 0.134i	55.4 + 7.8i	455	365	0.01	2.0	-864
1	0	1.014 - 0.170i	0.786 + 0.131i	-	688	141	0.35	-	-74
1	0.01	1.017 - 0.172i	0.789 + 0.128i	247 + 176i	686	141	0.35	0.4	-75
1	0.1	1.022 - 0.177i	0.794 + 0.120i	78.2 + 55.8i	683	140	0.34	1.4	-76
1	0.5	1.032 - 0.186i	0.802 + 0.105i	35.0 + 24.9i	676	138	0.32	3.2	-78
1	1	1.040 - 0.193i	0.809 + 0.093i	24.7 + 17.6i	671	137	0.31	4.5	-80
1	2	1.050 - 0.203i	0.819 + 0.077i	17.5 + 12.5i	665	136	0.30	6.4	-82
1	10	1.092 - 0.253i	0.859 + 0.046i	7.82 + 5.53i	639	129	0.23	14.2	-94

TABLE 2. Properties of the Kelvin mode, for different values of r^* and ν^* , relative to the reference values in table 1. For $\nu^* = 0$, the coefficient β_0 and hence the boundary-layer thickness δ_{lat}^* do not exist.

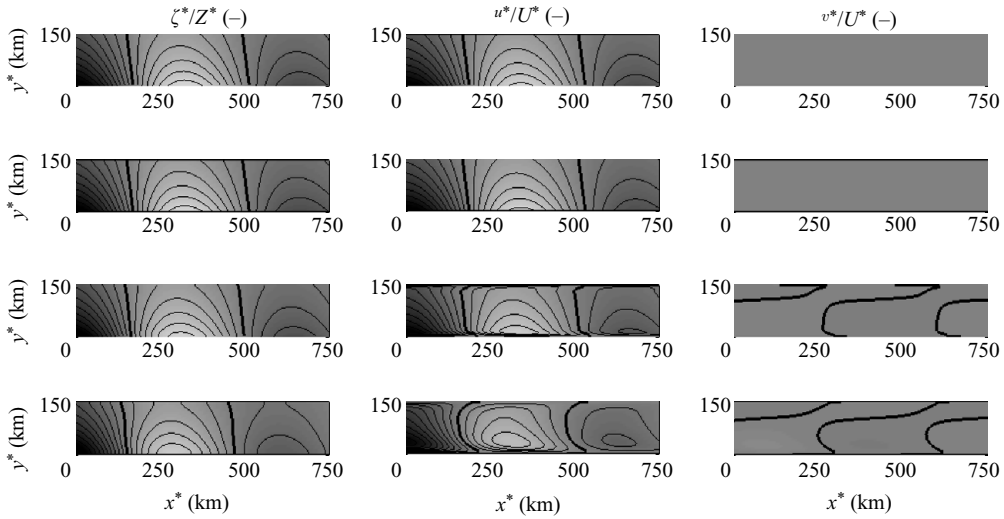


FIGURE 3. Viscous Kelvin wave, propagating to the right, showing snapshots of the surface elevation ζ (left), along-channel flow u (middle) and cross-channel flow v (right): top row, no dissipation ($r^* = v^* = 0$); second row, friction only ($v^* = 0$); third row, reference case; bottom row, exaggerated viscosity ($v^* = 10v_{ref}^*$). All other parameter values are as in table 1. Light shades indicate positive elevations/velocities and dark shades negative elevations/velocities. The thick line is the zero contour. Note that visualizing these wave modes does not require any boundary conditions at the left and right boundaries of the plotting domain.

First, the wavelength L^* and the Rossby deformation radius R^* (which is the e -folding length scale of cross-channel amplitude decay) are given by

$$L^* = \frac{2\pi}{K^* k_{0,re}}, \quad R^* = \frac{1}{K^* \alpha_{0,re}}, \quad (4.2)$$

respectively. As shown in table 2, both viscosity and bottom friction cause a decrease in tidal wavelength (increase in $k_{0,re}$) and therefore also a decrease in wave speed. The effects on the Rossby deformation radius are different: viscous effects lead to a decrease in R^* , and bottom friction leads to an increase in R^* .

Both dissipation mechanisms introduce amplitude decay in the direction of propagation, which is reflected in the wavenumber becoming a complex quantity ($k_{im} < 0$). To quantify the decay, we define the factor D as the ratio of the wave amplitudes at two locations separated by one wavelength in the longitudinal direction:

$$D = \exp\left(\frac{2\pi k_{0,im}}{k_{0,re}}\right). \quad (4.3)$$

In the absence of dissipation, one obtains $D = 1$; viscous effects and bottom friction lead to $D < 1$ (table 2).

The most striking property of the viscous Kelvin mode is the presence of two boundary layers along the channel boundaries $y = 0, B$, in which flow velocities go to zero (figure 3). They are associated with the terms proportional to $\exp(-\beta y)$ and $\exp(\beta[y - B])$ in (3.4). The boundary-layer thickness δ_{lat}^* can now be quantified

as an e -folding length scale according to

$$\delta_{lat}^* = \frac{1}{K^* \beta_{0,re}}, \quad (4.4)$$

which gives a value of 4.5 km in the reference case. As shown in table 2, increasing bottom friction leads to a decrease in boundary-layer thickness, while increasing the eddy viscosity leads to an increase in boundary-layer thickness. These qualitative properties are confirmed when we approximate δ_{lat}^* by considering only the leading term of β_0 according in expansion (3.10). Using Appendix A, (4.4) then reduces to the classical Stokes formula (Batchelor 1967) with a friction-induced correction factor μ :

$$\delta_{lat}^* \approx \frac{1}{K^* [\beta_{0,-1} v^{-1/2}]_{re}} = \frac{v^{1/2}}{K^* [\gamma \sqrt{i}]_{re}} = \mu \sqrt{\frac{2v^*}{\sigma^*}}, \quad \mu = \sqrt{\sqrt{1+r^2} - r}. \quad (4.5)$$

The boundary layers have two further properties: a phase lead of the along-channel flow with respect to the surface elevation and a small cross-channel flow component, of order $v^{1/2}$. Bottom friction also introduces a slight phase lead of the flow field with respect to the surface elevation but no cross-channel flow component. Furthermore, due to viscous effects, the Kelvin wave solution is no longer independent of the channel width (which is typical for the inviscid case).

Finally, the last column of table 2 characterizes the amphidromic system created by two Kelvin waves, travelling in opposite directions. As we will see in § 5, this system typifies the Taylor solution sufficiently far away from the basin's closed end (provided that all reflected Poincaré modes are evanescent; see § 4.3). The amphidromic points are found on a line making an angle with the longitudinal boundaries. As shown in Appendix B, the lateral displacement of two neighbouring amphidromic points is given by

$$\Delta y_{amph}^* = \frac{\pi}{K^* k_{0,re}} \frac{k_{0,im}}{\alpha_{0,re}}. \quad (4.6)$$

For the cases either without friction or without viscosity, this expression can be further elaborated (Appendix B). The negative values in table 2 indicate that subsequent amphidromes, viewed in the direction of propagation, are closer to the coastline to which the Kelvin wave is bound. The effects of two types of dissipation on the amphidromic system of two Kelvin waves are qualitatively similar: increasing dissipation causes an increase in Δy_{amph}^* .

4.3. Viscous Poincaré modes

In the inviscid and frictionless case, Poincaré modes are either free/unbound (wavenumber k_m is real) or evanescent/bound (wavenumber is purely imaginary). A critical value of the basin width exists,

$$B_{cr}^* = \pi \sqrt{\frac{g^* H^*}{\sigma^{*2} - f^{*2}}}, \quad (4.7)$$

such that for $B^* < B_{cr}^*$ all modes are evanescent, whereas for $B^* > B_{cr}^*$ a finite number of modes is free and all others are evanescent. For the parameter values in table 1, the basin width ($B^* = 150$ km) is well below the critical value ($B_{cr}^* = 608$ km), so all Poincaré modes turn out to be evanescent. Note that for a fixed basin width B^* , one may equivalently derive a critical tidal frequency σ_{cr}^* , a critical water depth H_{cr}^* (Hendershott & Speranza 1971) or a critical tidal period T_{cr}^* (Brown 1973), such that all Poincaré modes are evanescent for $\sigma^* < \sigma_{cr}^*$, $H^* > H_{cr}^*$ or $T^* > T_{cr}^*$.

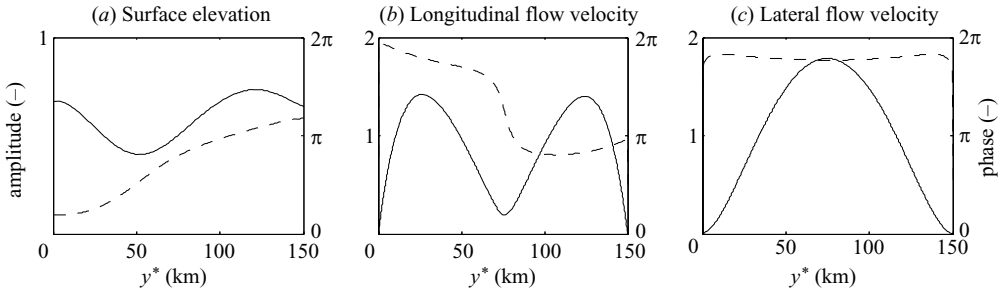


FIGURE 4. Lateral structure of the lowest viscous Poincaré mode ($m = 1$) showing amplitude (solid line) and phase (dashed line) of three dimensionless quantities: (a) free-surface elevation $\hat{\zeta}$, (b) longitudinal flow velocity \hat{u} and (c) lateral flow velocity \hat{v} . Parameter values are as in table 1.

The introduction of horizontally viscous effects (and, also, bottom friction; e.g. see Sinha & Pingree 1997) somewhat complicates the classification into free and evanescent modes. The free modes now display a slight decay in the direction of propagation (wavenumber obtains a non-zero imaginary part), whereas the evanescent modes obtain a slightly propagative character (wavenumber obtains a non-zero real part; see figure 2). However, for small values of $\nu^{1/2}$ and r , these modifications are small, and it is useful to refer to the inviscid and frictionless case to classify a mode as free or as evanescent. The e -folding decay length, given by

$$L_m^* = \frac{1}{K^* |k_{m,im}|}, \quad (4.8)$$

equals 48 km for the lowest mode, which is slightly smaller than its inviscid counterpart (50 km, parameter values as in table 1). In general, viscous effects are found to reduce the e -folding length scale of along-channel decay for the evanescent modes or the wavelength of the free modes. These observations hold for the higher Poincaré modes, as well.

Just like the viscous Kelvin wave, the viscous Poincaré modes also have boundary layers along $y = 0$ and $y = B$, in first approximation also satisfying Stokes formula with correction factor μ as given in (4.5). These boundary layers can for example be seen in figure 4(b), which shows the lateral structure of the longitudinal velocity of the lowest Poincaré mode.

4.4. New type of mode

For each viscous Poincaré mode, we additionally find a new mode with a roughly similar lateral structure. We emphasize that these modes entirely owe their existence to the presence of horizontally viscous effects; for $\nu^* = 0$ they do not exist. The new modes are all evanescent, with an e -folding decay length L_{-m}^* defined analogous to (4.8). The along-channel e -folding decay length is bounded by

$$\delta_{long}^* = \frac{1}{K^* |k_{-1,im}|} \approx \frac{\nu^{1/2}}{K^* \left| \left[\gamma \sqrt{-i} \right]_{im} \right|} = \mu \sqrt{\frac{2\nu^*}{\sigma^*}}, \quad \mu = \sqrt{\sqrt{1+r^2} - r}. \quad (4.9)$$

In this approximation, we have used the leading term of k_0 according to expansion (3.8) and Appendix A. Just like the boundary-layer thickness of the Kelvin and Poincaré

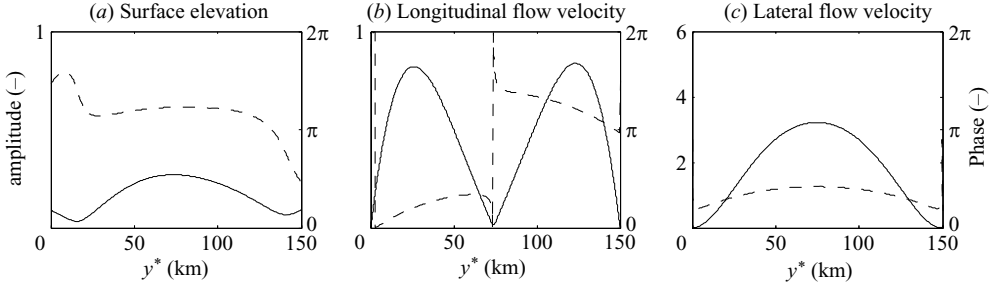


FIGURE 5. Same as figure 4, but now for the lowest new type of mode ($m = -1$).

modes, this result satisfies Stokes boundary-layer formula, with the same friction-induced correction factor μ as already given in (4.5).

Finally, let us compare the lateral structure of the lowest new mode (figure 5) with that of the lowest viscous Poincaré mode (figure 4). The components of the flow field have a similar structure: their absolute values (solid line) show a similar pattern, whereas the phase curves (dashed line) are roughly inverted. Please note the difference in strength of the lateral and the longitudinal flow component of the new mode. The lateral structures of the free-surface elevation look rather different, with the phase of the Poincaré mode clearly showing the (Coriolis-induced) propagation in the negative y -direction.

5. Results: solution to the viscous Taylor problem

5.1. Superposition of normal modes: Galerkin approach

Now let us turn to the viscous Taylor problem, with the semi-enclosed basin geometry depicted in figure 1(b) and an incoming Kelvin wave from $+\infty$. The key step is to write the solution as a superposition of the normal modes, derived in §3 and analysed in §4. We thus consider a truncated sum of an incoming Kelvin wave, a reflected Kelvin wave, M Poincaré modes and M new modes:

$$\phi = \hat{\phi}_0^{inc}(y) \exp(i[t + k_0 x]) + \sum_{m=-M}^M C_m \hat{\phi}_m(y) \exp(i[t - k_m x]) + \text{c.c.}, \quad (5.1)$$

with

$$\hat{\phi}_0^{inc}(y) = (\hat{\zeta}_0(B - y), -\hat{u}_0(B - y), -\hat{v}_0(B - y)). \quad (5.2)$$

Recall that the Kelvin mode is denoted by the subscript $m = 0$, whereas Poincaré modes are denoted by $m > 0$ and the new modes by $m < 0$. The first term in (5.1), further detailed in (5.2), corresponds to the incoming Kelvin wave (based on the symmetry properties mentioned in §3). The incoming Kelvin wave travels in the negative x -direction, and its amplitude has been fixed to unity at $x = 0$. (Note that in the inviscid case, the new type of mode does not exist and the summation in (5.1) would be from $m = 0$ to $m = M$, including only inviscid Kelvin and Poincaré modes.)

The above solution involves $2M + 1$ complex coefficients C_m , to be determined from the no-slip boundary condition along the lateral basin boundary $x = 0$. To this end, various methods can be used. We follow a Galerkin approach, which minimizes a residual ϵ that, according to the no-slip boundary condition at the closed end, should

be zero:

$$\epsilon = \frac{1}{B} \int_0^B (|u(0, y)|^2 + |v(0, y)|^2) dy. \tag{5.3}$$

Minimizing ϵ implies that all partial derivatives of ϵ with respect to the coefficients C_m must vanish. We thus obtain the following set of $2M + 1$ equations:

$$\sum_{n=-M}^M [C_n \int_0^B (\hat{u}_n \hat{u}_m + \hat{v}_n \hat{v}_m) dy] = - \int_0^B (\hat{u}_{inc} \hat{u}_m + \hat{v}_{inc} \hat{v}_m) dy, \tag{5.4}$$

for $m = -M, \dots, M$. The inviscid counterpart of the above is obtained by removing the v -terms from (5.3) and (5.4). The linear set of equations (5.4) is solved by means of a standard method.

(Alternatively, one may adopt a collocation technique. In the viscous case, however, this method is rather sensitive to the choice of collocation points and constraints. The following procedure turns out to work, but not better than Galerkin. Define equidistant collocation points $y_n = nB/(2M + 2)$, and require the longitudinal velocity to vanish at $M + 1$ points with an odd index and the lateral velocity to vanish at M points with an even index ($n = 1, 2, \dots, 2M + 1$.)

5.2. Properties of the solution

Figure 6 shows the amphidromic system, obtained using the Galerkin method with $M = 12$, for different parameter settings. Details of the flow field in the lower left corner of the domain are shown, as well. The viscous solution clearly displays boundary layers, along the longitudinal coastlines $y = 0, B$ as well as along the transverse one at $x = 0$. The latter boundary layer is due to the new type of mode, as described in §4.4.

Now let us turn to the details of the amphidromic system. Sufficiently far away from the closed basin boundary (and, additionally, if $B < B_{cr}$ such that all reflected modes are evanescent), the solution shows amphidromic points on a line, making an angle with the longitudinal direction (figure 6). In the absence of dissipation, i.e. for $r^* = v^* = 0$, this line coincides with the centreline of the basin (figure 6a). This property can be explained by noting that the far-field Taylor solution is characterized by the superposition of two Kelvin waves: an incoming one and a reflected one. In §4.2, we already investigated the effects of dissipation on such a system of two Kelvin waves (also see Appendix B). We conclude that the horizontal eddy viscosity has a similar effect on the amphidromic points as bottom friction (Hendershott & Speranza 1971; Rienecker & Teubner 1980; Rizal 2002).

For a channel width exceeding the critical value, the amphidromic system is more complicated. Analogous to the inviscid case, the far-field solution then also contains a finite number of free Poincaré modes. The amphidromic points then result from a complex interference pattern of the two Kelvin waves mentioned above and the free Poincaré modes, which have a wavelength much larger than that of the Kelvin mode.

5.3. Comparison with observations

Now we will compare our idealized model results with observations in the Southern Bight of the North Sea. Tidal amplitudes and phases of the semidiurnal lunar tide are available from various stations along the English, French, Belgian and Dutch coasts (Sinha & Pingree 1997; RIKZ 2002).

Our procedure consists of the following steps. A rectangular basin geometry is drawn that, upon visual inspection, provides the best match with the coastlines in

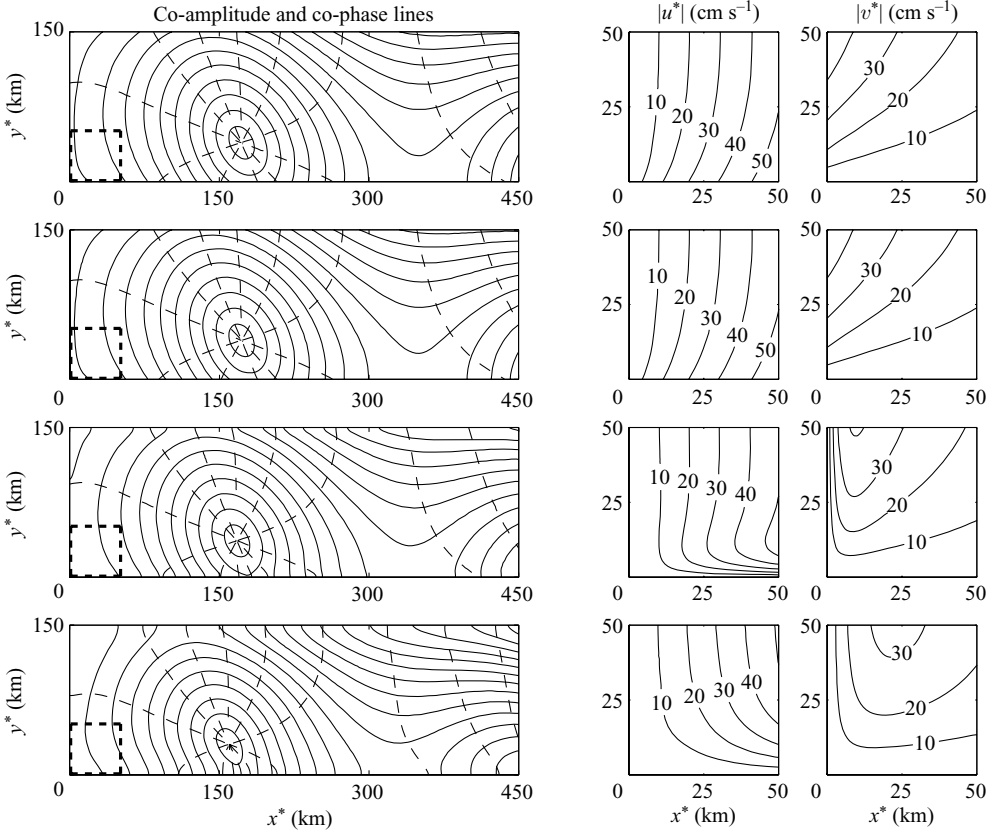


FIGURE 6. Taylor solution, for different parameter settings: top row, no dissipation ($r^* = v^* = 0$); second row, friction only ($v^* = 0$); third row, reference case; bottom row, exaggerated viscosity ($v^* = 10v_{ref}^*$). Other parameter values are as in table 1, with truncation number $M = 12$. The leftmost plots show co-amplitude lines (solid lines, with an interval of 20 cm) and co-phase lines (dashed lines, dividing the tidal period into 12 intervals). To visualize the boundary layers in the lower left corner, the two plots on the right show the longitudinal and lateral flow amplitudes.

the Southern Bight (150 km \times 150 km; see figure 7a). Next, the location of each tide station, inside or outside the model basin, is projected orthogonally on to the nearest basin boundary. The tide stations thus become points along the perimeter of the model basin, which allows us to compare results and observations as a function of a one-dimensional perimeter coordinate. Model runs are then performed for fixed values of the water depth, Coriolis parameter, bottom-friction coefficient and horizontal eddy viscosity (table 1, using the Galerkin approach with truncation number $M = 12$). Although not systematically, we have varied the amplitude and phase shift of the incoming Kelvin wave to obtain a best fit with the observations.

The basin geometry, the tide stations and the model results are shown in figure 7. The tidal phase shows good agreement between model and observations, except in the western corner near the outflow of the river Thames. The agreement with respect to amplitude is somewhat poorer but qualitatively reasonable. Adding a realistic horizontal viscosity does not improve the fit.

Note that a fit with two Kelvin waves only, as done by Hendershott & Speranza (1971) for the Adriatic Sea and the Gulf of California, is inadequate here. Our focus

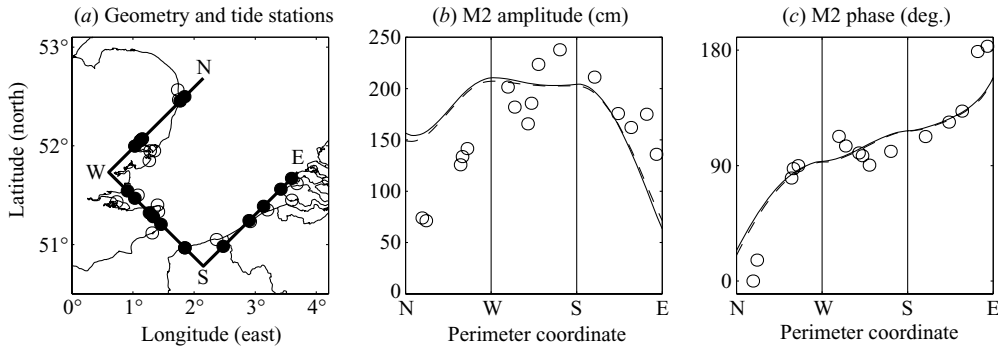


FIGURE 7. Comparison between model results and tide observations in the Southern Bight of the North Sea: (a) model geometry and tide gauge stations (open circles, original locations; filled circles, projected), (b) M2 amplitude and (c) M2 phase. Both the model results (solid line, viscous; dashed line, inviscid) and the observations (circles) are plotted as a function of the perimeter coordinate. Parameter values are as in table 1 ($M = 12$).

is on tide propagation along or near the basin's closed end, where Poincaré modes are crucial. Furthermore, the contribution of the lowest Poincaré mode is felt in the interior of the basin, since the e -folding decay length (48 km; see §4.3) is not small compared to the basin length (150 km). The following factors, not accounted for in our idealized model, complicate the above comparison: (i) complex coastline and slight funnel shape; (ii) connections to other waters, mainly the Dover Strait (see Brown 1987, 1989) but also the river Thames and Western Scheldt; (iii) non-uniform bottom topography; and (iv) the open boundary to the north.

The qualitative properties of tide propagation in the Southern Bight of the North Sea are fairly reproduced by the idealized model. Accurate quantitative agreement, however, cannot be expected in view of the complicated setting.

6. Conclusions

We have solved the viscous Taylor problem; i.e. we have extended the original Taylor (1921) problem of Kelvin wave reflection in a semi-enclosed basin to account for horizontally viscous effects. The solution, written as a truncated sum of normal modes, involves three types of wave solutions in an infinite channel: viscous counterparts of the Kelvin and Poincaré modes, as well as a new type of mode. Each of these modes displays boundary layers, with a thickness that can be approximated by Stokes' formula, modified by a friction-induced correction factor. The longitudinal length scales of the viscous Kelvin and Poincaré modes (wavelength for the free modes, e -folding decay distance for the evanescent modes) are smaller than in the inviscid case, an effect also caused by bottom friction. Contrary to bottom friction, viscous effects lead to a decrease in Rossby deformation radius. The new type of mode are all evanescent waves, with an e -folding decay distance that can be approximated by the same modified Stokes' formula mentioned above.

The solution is then written as a superposition of these normal modes: an incoming Kelvin wave and a truncated sum of reflected modes. A Galerkin technique is applied to satisfy no slip at the basin's closed boundary. The solution shows boundary layers along the longitudinal boundaries as well as along the basin's closed end, the latter created by the new type of mode, and amphidromic points on a line making an angle with the longitudinal direction.

We conclude that the introduction of a horizontal eddy viscosity affects both the qualitative and quantitative properties of the Taylor solution and the underlying normal modes. Parameter values typical for the Southern Bight of the North Sea suggest that the quantitative aspects are dominated by bottom friction rather than by viscous effects. Using these values and approximating the Southern Bight with a rectangular embayment, the qualitative properties of tide propagation are reasonably well reproduced by the idealized model.

This work is supported by the Netherlands Technology Foundation STW, the applied science division of NWO and the Netherlands Ministry of Economic Affairs. We thank three anonymous reviewers for their comments.

Appendix A. Details of the expansion in powers of $\nu^{1/2}$

A.1. Introduction

This section contains the details of the expansion in powers of $\nu^{1/2}$, as shown in (3.8)–(3.10). First recall that the three equations are the α -expression, the β -expression and the solvability condition, given by

$$a\alpha^4 + b\alpha^2 + c = 0, \quad a\beta^4 + b\beta^2 + c = 0, \quad \det \mathbf{A} = 0, \quad (\text{A } 1)$$

respectively. The coefficients a , b and c have been specified in (3.3), and the matrix \mathbf{A} has been specified in (3.5). Considering the α -expression at $O(\nu^{-1})$, we obtain

$$k_{m,-1}^2(k_{m,-1}^2 + \gamma^2 i) = 0. \quad (\text{A } 2)$$

The different roots of this equation now lead to two different classes of wave solutions: the double root $k_{m,-1} = 0$ corresponds to the viscous Kelvin and Poincaré modes, whereas the two roots $k_{m,-1}^2 = -\gamma^2 i$ correspond to the new type of modes, left bound and right bound. By symmetry, it suffices to consider only wavenumbers with a negative or zero imaginary part.

A.2. Viscous Kelvin and Poincaré modes

First, let us investigate the root $k_{m,-1} = 0$. The β -expression, subsequently evaluated at $O(\nu^{-1})$ and $O(\nu^{-1/2})$, now leads to

$$\beta_{m,-1}^2[\beta_{m,-1}^2 - i\gamma^2] = 0, \quad (\text{A } 3)$$

$$2\beta_{m,0}\beta_{m,-1}[2\beta_{m,-1}^2 - i\gamma^2] = 0, \quad (\text{A } 4)$$

which leads to $\beta_{m,-1} = \gamma\sqrt{i}$ (assuming $\beta_{m,-1}$ to be non-zero – otherwise, α_m and β_m become identical) and $\beta_{m,0} = 0$. Next, the α -expression at $O(\nu^0)$ and the solvability condition at $O(\nu^{-1})$ give a coupled set of equations for k_0 and α_0 :

$$(f^2 k_{m,0}^2 - \gamma^4 \alpha_{m,0}^2) \sin(i\alpha_{m,0} B) = 0, \quad (\text{A } 5)$$

$$k_{m,0}^2 - \alpha_{m,0}^2 + f^2/\gamma^2 - \gamma^2 = 0. \quad (\text{A } 6)$$

Here we simply find the characteristics of the inviscid Kelvin mode ($k_{m,0} = \gamma$, $\alpha_{m,0} = f/\gamma$) and Poincaré modes ($\alpha_{m,0} = m\pi i/B$, $k_{m,0} = [\gamma^2 - (f/\gamma)^2 - (m\pi/B)^2]^{1/2}$, for $m = 1, 2, \dots$), both including bottom friction (Rienecker & Teubner 1980).

Next, $\beta_{m,1}$ is determined from the β -expression at $O(\nu^0)$. The coefficients $k_{m,1}$ and $\alpha_{m,1}$ are obtained from combining the α -expression at $O(\nu^{1/2})$ and the solvability condition at $O(\nu^{-1/2})$ (see table 3). Repeating this loop at increasing powers of $\nu^{1/2}$, one may subsequently obtain $(\beta_{m,2}, k_{m,2}, \alpha_{m,2})$, $(\beta_{m,3}, k_{m,3}, \alpha_{m,3})$ and so forth.

	α -expression	β -expression	Solvability condition	Result(s)
1.	–	$O(v^{-1})$	–	$\beta_{0,-1} = \gamma\sqrt{i}$
2.	–	$O(v^{-1/2})$	–	$\beta_{0,0} = 0$
3.	$O(v^0)$	–	$O(v^{-1})$	$\alpha_{0,0} = \mathcal{F}$ $k_{0,0} = \gamma$
4.	–	$O(v^0)$	–	$\beta_{0,1} = (\gamma^2 - \mathcal{F}^2)/(2\beta_{0,-1})$
5.	$O(v^{1/2})$	–	$O(v^{-1/2})$	$\alpha_{0,1} = \gamma^2 \coth(\mathcal{F}B)/\beta_{0,-1}$ $k_{0,1} = f \coth(\mathcal{F}B)/\beta_{0,-1}$
<hr/>				
1.	–	$O(v^{-1})$	–	$\beta_{m,-1} = \gamma\sqrt{i}$
2.	–	$O(v^{-1/2})$	–	$\beta_{m,0} = 0$
3.	$O(v^0)$	–	$O(v^{-1})$	$\alpha_{m,0} = m\pi i/B$ (for $m = 1, 2, \dots$) $k_{m,0}^2 = \gamma^2 - \mathcal{F}^2 + \alpha_{m,0}^2$ (take root with imaginary part ≤ 0)
4.	–	$O(v^0)$	–	$\beta_{m,1} = (k_{m,0}^2 - \mathcal{F}^2)/(2\beta_{m,-1})$
5.	$O(v^{1/2})$	–	$O(v^{-1/2})$	$\alpha_{m,1} = (2k_{m,0}^2\alpha_{m,0})/(\beta_{m,-1}B[\alpha_{m,0}^2 - \mathcal{F}^2])$ $k_{m,1} = (2k_{m,0}\alpha_{m,0}^2)/(\beta_{m,-1}B[\alpha_{m,0}^2 - \mathcal{F}^2])$
<hr/>				
1.	$O(v^{-1})$	–	–	$k_{m,-1} = \gamma\sqrt{-i}$
2.	–	$O(v^{-1})$	–	$\beta_{m,-1} = \gamma\sqrt{-i}$
3.	$O(v^{-1/2})$	–	–	$k_{m,0} = 0$
4.	–	$O(v^{-1/2})$	–	$\beta_{m,0} = 0$
5.	–	–	$O(v^{-2})$	$\alpha_{m,0} = m\pi i/B$ (for $m = -1, -2, \dots$)
6.	$O(v^0)$	–	–	$k_{m,1} = (\mathcal{F}^2 + \alpha_{m,0}^2)/(2k_{m,-1})$
7.	–	$O(v^0)$	–	$\beta_{m,1} = (2\mathcal{F}^2 + \alpha_{m,0}^2 - \gamma^2)/(2\beta_{m,-1})$
8.	–	–	$O(v^{-3/2})$	$\alpha_{m,1} = 2\alpha_{m,0}/(\beta_{m,-1}B)$

TABLE 3. Expansion coefficients for α_m , β_m and k_m corresponding to the viscous Kelvin mode (top, $m = 0$), the viscous Poincaré modes (middle, $m > 0$) and the new type of modes (bottom, $m < 0$). Notation: $\mathcal{F} = f/\gamma$.

A.3. New modes

Now let us proceed with the second root of (A 2), namely $k_{m,-1} = \gamma\sqrt{-i}$. Evaluating the α -expression at $O(v^{-1/2})$ gives

$$k_{m,-1}k_{m,0}(2k_{m,-1}^2 + \gamma^2i) = 0, \tag{A 7}$$

which leads to $k_{m,0} = 0$. Considering the β -expression at $O(v^{-1})$ and at $O(v^{-1/2})$ while requiring $\beta_{m,-1} \neq 0$, we now obtain $\beta_{m,-1} = k_{m,-1}$ and $\beta_{m,0} = 0$. Using these results in the solvability condition at $O(v^{-2})$ gives

$$(\gamma^4 - f^2) \sin(i\alpha_{m,0}B) = 0. \tag{A 8}$$

This leads to $\alpha_{m,0} = m\pi i/B$ for $m = -1, -2, \dots$, which is identical to the Poincaré case, thus emphasizing that for each viscous Poincaré mode a new mode can be found. Furthermore, it is apparent that there is no such equivalent of the viscous Kelvin mode.

Next, subsequently considering the α -expression at $O(v^0)$, the β -expression at $O(v^0)$ and the solvability condition at $O(v^{-3/2})$ allows us to obtain $k_{m,1}$, $\beta_{m,1}$ and $\alpha_{m,1}$, respectively (see table 3). Repeating this loop at increasing powers of $v^{1/2}$, one may subsequently obtain $(k_{m,2}, \beta_{m,2}, \alpha_{m,2})$, $(k_{m,3}, \beta_{m,3}, \alpha_{m,3})$ and so forth.

Appendix B. Amphidromic system of two Kelvin waves

The free-surface elevation of an incoming Kelvin wave (propagating to the left) and a reflected Kelvin wave (with complex amplitude C_0 , propagating to the right) is given by

$$\zeta(x, y, t) = \hat{\zeta}(B - y) \exp(i[t + k_0x]) + C_0 \hat{\zeta}(y) \exp(i[t - k_0x]) + \text{c.c.} \quad (\text{B } 1)$$

Equating the absolute values of the two wave contributions in (B 1) leads to a necessary but not sufficient condition for the amphidromic points:

$$\exp(2k_{0,im}x) = \frac{|\hat{\zeta}(B - y)|}{|C_0 \hat{\zeta}(y)|}. \quad (\text{B } 2)$$

Independent of C_0 , this result simplifies to a straight line for those regions in which the lateral structure of the Kelvin wave is dominated by a single exponential term, i.e. where $\hat{\zeta}(y) \approx Z_1 \exp(-\alpha y)$. This condition is exactly satisfied by the inviscid Kelvin wave; it is approximately satisfied in the interior region of the viscous Kelvin wave, i.e. well away from the two boundary layers. The lateral displacement of two neighbouring amphidromic points is then given by (4.6) in §4.2. In the general case of arbitrary r and ν further elaboration of (4.6) is rather cumbersome. However, by isolating the two dissipation mechanisms, we find

$$r = 0: \quad \Delta y_{amph}^* = -\frac{\pi}{K^*} \sqrt{\frac{\nu}{2}} \coth(fB) + O(\nu), \quad (\text{B } 3)$$

$$\nu = 0: \quad \Delta y_{amph}^* = -\frac{\pi}{K^*} \frac{\xi \sqrt{2(\xi - 1)}}{f(\xi + 1)}, \quad \xi = \sqrt{1 + r^2}, \quad (\text{B } 4)$$

respectively. In (B 3), we have used Appendix A. Equation (B 4) confirms the findings by Rizal (2002), who identified the amphidromic points in the inviscid (but frictional) Taylor solution using a numerical search routine.

REFERENCES

- BACHELOR, G. K. 1967 *An Introduction to Fluid Dynamics*. Cambridge University Press.
- BROWN, P. J. 1973 Kelvin-wave reflection in a semi-infinite canal. *J. Mar. Res.* **31** (1), 1–10.
- BROWN, T. 1987 Kelvin wave reflection at an oscillating boundary with applications to the North Sea. *Cont. Shelf Res.* **7** (4), 351–365.
- BROWN, T. 1989 On the general problem of Kelvin wave reflection at an oscillating boundary. *Cont. Shelf Res.* **9** (10), 931–937.
- CAI, S. C., LONG, X., LIUB, H. & WANGA, S. 2006 Tide model evaluation under different conditions. *Cont. Shelf Res.* **26** (1), 104–112.
- CARBAJAL, N. 1997 Two applications of Taylor's problem solution for finite rectangular semi-enclosed basins. *Cont. Shelf Res.* **17** (7), 803–817.
- DAVEY, M. K., HSIEH, W. W. & WAJSOWICZ, R. C. 1983 The free Kelvin wave with lateral and vertical viscosity. *J. Phys. Oceanogr.* **13**, 2182–2191.
- DAVIES, A. M. & JONES, J. E. 1995 The influence of bottom and internal friction upon tidal currents: Taylor's problem in three dimensions. *Cont. Shelf Res.* **15** (10), 1251–1285.
- DAVIES, A. M. & JONES, J. E. 1996 The influence of wind and wind wave turbulence upon tidal currents: Taylor's problem in three dimensions with wind forcing. *Cont. Shelf Res.* **16** (1), 25–99.
- DYER, K. R. & HUNTLEY, D. A. 1999 The origin, classification and modelling of sand banks and ridges. *Cont. Shelf Res.* **19** (10), 1285–1330.

- FANG, G., KWOK, Y.-K., YU, K. & ZHU, Y. 1999 Numerical simulation of principal tidal constituents in the South China Sea, Gulf of Tonkin and Gulf of Thailand. *Cont. Shelf Res.* **19** (7), 845–869.
- HENDERSHOTT, M. C. & SPERANZA, A. 1971 Co-oscillating tides in long, narrow bays; the Taylor problem revisited. *Deep-Sea Res.* **18** (10), 959–980.
- LEBLOND, P. H. & MYSAK, L. A. 1978 *Waves in the Ocean*. Elsevier.
- PEDLOSKY, J. 1982 *Geophysical Fluid Dynamics*. Springer.
- PROUDMAN, J. 1941 The effect of coastal friction on the tides. *Mon. Not. R. Astron. Soc. Geophys. Suppl.* **1**, 23–26.
- RIENECKER, M. M. & TEUBNER, M. D. 1980 A note on frictional effects in Taylor's problem. *J. Mar. Res.* **38**, 183–191.
- RIJKSINSTITUUT VOOR KUST EN ZEE (RIKZ) 2002 *Getijtafels voor Nederland 2003* [in Dutch]. Sdu Uitgevers.
- RIPA, P. & ZAVALA-GARAY, J. 1999 Ocean channel modes. *J. Geophys. Res.* **104** (C7), 15 479–15 494.
- RIZAL, S. 2002 Taylor's problem – influences on the spatial distribution of real and virtual amphidromes. *Cont. Shelf Res.* **22** (15), 2147–2158.
- SINHA, B. & PINGREE, R. D. 1997 The principal lunar semidiurnal tide and its harmonics: baseline solutions for M2 and M4 constituents in the North-West European Continental Shelf. *Cont. Shelf Res.* **17** (11), 1321–1365.
- TAYLOR, G. I. 1921 Tidal oscillations in gulfs and rectangular basins. *Proc. Lond. Math. Soc.* **20**, 148–181.
- WINANT, C. D. 2007 Three-dimensional tidal flow in an elongated, rotating basin. *J. Phys. Oceanogr.* **37**, 2345–2362.
- XIA, Z., CARBAJAL, N. & SÜDERMANN, J. 1995 Tidal current amphidromic system in semi-enclosed basins. *Cont. Shelf Res.* **15** (2–3), 219–240.
- ZIMMERMAN, J. T. F. 1982 On the Lorentz linearization of a quadratically damped forced oscillator. *Phys. Lett. A* **89**, 123–124.